Electronic structure of the chiral helimagnet and 3*d*-intercalated transition metal dichalcogenide Cr$_{1/3}$NbS$_2$

N. Sirica,[1] S.-K. Mo,[2] F. Bondino,[3] I. Pis,[3,4] S. Nappini,[3] P. Vilmercati,[1] J. Yi,[6] Z. Gai,[7] P. C. Snijders,[8,1] P. K. Das,[3,5]
I. Vobornik,[3] N. Ghimire,[1] M. R. Koehler,[6] L. Li,[6] D. Sapkota,[1] D. S. Parker,[8] D. G. Mandrus,[1,6,8] and N. Mannella[1,*]

[1]*Department of Physics and Astronomy, The University of Tennessee, Knoxville, Tennessee 37996, USA*

[2]*Advanced Light Source, Lawrence Berkeley National Laboratory, Berkeley, California 94720, USA*

[3]*Istituto Officina dei Materiali (IOM)-CNR Laboratorio TASC, S.S. 14 Km 163.5, I-34149 Basovizza (TS), Italy*

[4]*Elettra-Sincrotrone Trieste S.C.p.A., S.S. 14 Km 163.5, I-34149 Basovizza (TS), Italy*

[5]*International Centre for Theoretical Physics, Strada Costiera 11, 34100 Trieste, Italy.*

[6]*Department of Materials Science and Engineering, The University of Tennessee, Knoxville, Tennessee 37996, USA*

[7]*Center for Nanophase Materials Sciences and Chemical Science Division, Oak Ridge National Laboratory, Oak Ridge,
Tennessee 37831, USA*

[8]*Materials Science and Technology Division, Oak Ridge National Laboratory, Oak Ridge, Tennessee 37831, USA*

The electronic structure of the chiral helimagnet Cr$_{1/3}$NbS$_2$ has been studied with core level and angle-resolved photoemission spectroscopy (ARPES). Intercalated Cr atoms are found to be effective in donating electrons to the NbS$_2$ layers but also cause significant modifications of the electronic structure of the host NbS$_2$ material. In particular, the data provide evidence that a description of the electronic structure of Cr$_{1/3}$NbS$_2$ on the basis of a simple rigid band picture is untenable. The data also reveal substantial inconsistencies with the predictions of standard density functional theory. The relevance of these results to the attainment of a correct description of the electronic structure of chiral helimagnets, magnetic thin films/multilayers, and transition metal dichalcogenides intercalated with 3*d* magnetic elements is discussed.

I. INTRODUCTION

Chiral helimagnets (CHMs) are ferromagnetic crystals belonging to chiral space groups, i.e., having a crystal structure lacking both a center of inversion, as well as a mirror plane [1]. When local spin moments are distributed on the chiral framework of the lattice, the resulting magnetization twists into a helix having a periodicity that can be tens of nanometers long. In this respect, CHMs are unique in that only right- or left-handed helices occur. This is in contrast to helical spin structures arising from crystals possessing a centrosymmetric space group, in which both right- and left-handedness coexist [2].

An interesting property of CHMs is that they support extremely stable solitons, i.e., nonlinear excitations that maintain their shape and energy as they propagate [3]. In particular, the observation of solitons in the form of two-dimensional vortices called skyrmions [4] in MnSi [5], Fe$_{1-x}$Co$_x$Si [6,7], FeGe [8,9], and Cu$_2$OSeO$_3$ [10] has attracted a great deal of attention towards CHM materials thanks to their promising spintronic functionalities. Due to the extremely long length scales of helical arrangements and skyrmions, the spin degrees of freedom can be manipulated at the nanoscale, and possibly even the mesoscopic level, independently of the details of the crystal structure. This allows for the possibility of manipulating skyrmions using magnetic fields or spin polarized currents [4,11,12]. Moreover, due to the fact that an electron traveling through a skyrmion acquires a Berry phase, skyrmions can have a profound effect on the electronic transport, as best exemplified by the topological Hall effect [13–15].

Most recently, another nontrivial, one-dimensional spin texture known as a chiral soliton lattice (CSL) has been observed in the CHM chromium-intercalated niobium disulfide (Cr$_{1/3}$NbS$_2$) [16]. Remarkably, the size and shape of the CLS can be controlled by varying the strength of a modest applied magnetic field (0.2 T) along the *ab* plane of the hexagonal crystal structure [16]. From a technological viewpoint, the CSL can be thought of as a tunable magnetic superlattice acting as an effective potential for itinerant electron spins [17]. Beyond the possibility of exercising precise control over the transport properties of spin carriers, the high stability and robustness of the CSL phase has made Cr$_{1/3}$NbS$_2$ an attractive candidate for a wide range of other spintronic applications [18–20].

Although the magnetic excitations, such as kinks, skyrmions, and CSL, which are at the heart of the functionality of CHMs, manifest on the nanoscale and possibly mesoscale level, their microscopic origin is found in the fundamental interactions allowed in a crystalline lattice lacking inversion symmetry. The microscopic ingredient underpinning the helical spin structures in CHMs is the antisymmetric spin interaction originating from a relativistic spin-orbit coupling known as the Dzyaloshinskii-Moriya interaction (DMI) [21–23]. The DMI originates as a first order correction to the energy of the superexchange Hamiltonian treating the spin-orbit coupling as a perturbation [22,23]. For crystals with a high degree of symmetry, this correction is very small, but it becomes the leading correction term when inversion symmetry is broken, as in CHM materials. The DMI is antisymmetric with respect to the exchange of two spins, in contrast to the more familiar direct exchange, which is symmetric. While the direct exchange leads to a parallel (ferromagnetic) or antiparallel (antiferromagnetic) orientation of the spins, the

*nmannell@utk.edu

DMI favors a perpendicular orientation of the spins. In CHMs, it is the competition between the symmetric ferromagnetic exchange and the much weaker antisymmetric DMI that twists the magnetization into a helix with a long periodicity [21,22,24–26].

With the DMI being rooted in the relativistic spin-orbit interaction (SOI) [22,23], a detailed knowledge of the electronic structure of available CHMs is necessary to elucidate the microscopic interactions underpinning their functional properties. Studies of the electronic structure of $Cr_{1/3}NbS_2$ are especially relevant as this compound can be considered a model system for studying the role played by the SOI in the DMI and how this relates to chiral helimagnetism. As compared to isotropic CHMs, such as MnSi, $Cr_{1/3}NbS_2$ is hexagonal and highly anisotropic [27]. This anisotropy provides the additional possibility of manipulating spin textures in $Cr_{1/3}NbS_2$ by applying a magnetic field along different crystallographic directions lying either parallel or perpendicular to the helical axis [28]. Due to the high anisotropy and the fact that inversion symmetry is broken only along one axis, $Cr_{1/3}NbS_2$ can also be considered an ideal system for the study of spin textures in magnetic thin films, devices fabricated on a substrate, and SOI coupling effects in magnetic multilayers [27]. Moreover, $Cr_{1/3}NbS_2$ is also a suitable material for investigating the interplay between transport and magnetic degrees of freedom [28–30].

Beyond its importance in the context of CHM materials, $Cr_{1/3}NbS_2$ is a compelling example of a transition metal dichalcogenide (TMDC) intercalated with a $3d$ magnetic element (Cr). Recently, group VI TMDCs have generated a great deal of interest in the community thanks to the possibility of manipulating valley spin or pseudo-spin using circularly polarized light [31–34]. Part of the broad appeal of layered TMDCs is that they are amenable to additional modification of their electronic structure [35]. One way this can be accomplished is through intercalation of a variety of electron donor species, ranging from alkali metals [36] to large organic molecules [37]. This drastically changes the carrier concentration of the host TMDC material and results in many nontrivial effects, including metal-to-semiconductor transitions [38], or semiconductor-to-superconductor transitions [39]. Consequently, given the potential technological application of layered TMDCs, it is important to develop a systematic understanding as to how intercalation serves to modify the electronic structure of the host material. In this regard, $Cr_{1/3}NbS_2$ serves as a prototypical case study of intercalation of TMDCs with $3d$ magnetic atoms.

In this paper, we report a comprehensive study of the electronic structure of $Cr_{1/3}NbS_2$ using core level photoemission (PES) and angle-resolved photoemission spectroscopy (ARPES). To obtain data representative of different probing depths, the ARPES data were taken with photon energies $h\nu = 40$ and 48 eV, as in conventional ARPES experiments and with photons of higher energies, ranging from $h\nu = 196$ eV to $h\nu = 736$ eV, in a regime that is hereafter referred to as soft x-ray ARPES (SX-ARPES). Although intercalation of Cr atoms was found to result in electronic charge donation to the NbS_2 layers, the data reveal a significant modification of the electronic structure of NbS_2 beyond what is expected from a simple rigid band picture. Specifically, as compared

to NbS_2, the data in $Cr_{1/3}NbS_2$ reveal (i) the presence of two additional bands at $\Gamma(\beta_{1,2})$ and two additional bands at $K(\delta_{1,2})$, (ii) a splitting of the antibonding band (α) derived from NbS_2, and (iii) an inversion of the energy hierarchy of the a_1' state (with symmetry d_{z^2}) and the e' states ($d_{x^2-y^2}/d_{xy}$) in the D_{3h} manifold of the trigonal prismatic environment of the Nb atom. The data further indicate a very weak k_z dispersion, and that the proper Brillouin zone (BZ) for $Cr_{1/3}NbS_2$ is the (1×1) BZ of NbS_2, suggesting a weak interlayer coupling and challenging the results of recent density functional theory (DFT) calculations.

The organization of the paper is as follows: To provide the proper context of our experimental results, we first present a brief review of the crystal and electronic structure of $Cr_{1/3}NbS_2$ and intercalated TMDCs, in general. After the Experimental Details and Methods section, the results are presented. A characterization of the $Cr_{1/3}NbS_2$ surface is discussed first, followed by a direct comparison of ARPES data in $Cr_{1/3}NbS_2$ and NbS_2, and a discussion of polarization-dependent ARPES data in $Cr_{1/3}NbS_2$. The last section provides a summary of the results of this study.

II. CRYSTAL AND ELECTRONIC STRUCTURE OF CHROMIUM INTERCALATED NIOBIUM DISULFIDE $Cr_{1/3}NbS_2$

The $Cr_{1/3}NbS_2$ crystallizes in the $Nb_3CoS_6(hP20)$ structure type ($P6_322$ space group). It is a TMDC, with intercalated Cr atoms ordering in a $(\sqrt{3}\times\sqrt{3})R(30°)$ superstructure, occupying octahedral (O_h) sites within the van der Waal gaps of the $2H$ poly-type structure of NbS_2 ($2H$-NbS_2) [40]. Such an ordering is a consequence of the stacking arrangement defined by the $2H$-NbS_2 structure. Within the $2H$ poly-type, each Nb atom can be found in a local, trigonal prismatic environment coordinated by six S atoms [41]. Adjacent NbS_2 layers are rotated by 60° with respect to one another producing empty, O_h hole sites in which the Cr atoms intercalate [42]. The unit cell of $Cr_{1/3}NbS_2$, with lattice constants $a = b = 5.741$ Å and $c = 12.101$ Å, contains 20 atoms, with 12 S atoms occupying the general site and six Nb atoms in two inequivalent positions [29].

Cr local spin moments order ferromagnetically in the ab plane below the Curie temperature $T_C = 116$-132 K [29,30,43,44]. Static susceptibility measurements demonstrate a Curie-Weiss behavior in which the effective moment is consistent with that of a local, spin derived moment originating from Cr being in a Cr^{3+} oxidation state [29]. This is further supported by the saturation of the magnetization at $3 \mu_B/Cr$, suggesting that the Cr atoms adopt a high spin configuration in its trigonally distorted O_h crystal field [29].

To describe the electronic structure of intercalated TMDC, it is proper to first discuss the electronic structure of the parent TMDC compound. While few reports of $2H$-NbS_2 have appeared, the isostructural and isoelectronic compound $2H$-$NbSe_2$ is in contrast very well studied. Thus, a description of the electronic structure of $2H$-$NbSe_2$ will be presented below under the supposition that there are only minor differences as compared to that of NbS_2.

Ab initio DFT calculations for $2H$-$NbSe_2$ have shown a grouping of the Nb d bands to be roughly consistent with that of a simplified ligand field model [45]. Here, the Nb atom ($4d^1$)

sits in a trigonal prismatic environment (D_{3h}), in which the crystal field splits the fivefold degenerate Nb $4d$ states into one singly degenerate a_1' state with symmetry z^2 and two doubly degenerate e' and e'' states with symmetry $x^2 - y^2/xy$, and xz/yz, respectively [1]. The relative energies of these states is dictated by the overlap of the Nb $4d$ and the Se $3p$ states. Since the ligands are situated at the corners of the prism, a greater Coulomb repulsion results from an increased orbital overlap between the e'' states (d_{xz}/d_{yz}), with the ligand (Se) p states. Consequently, the e'' states are raised in energy relative to the e' ($d_{x^2-y^2}/d_{xy}$) and a_1' (d_{z^2}) states. Moreover, given the larger distance separating neighboring Nb atoms along the c axis, the a_1' (d_{z^2}) states are lower in energy than the e' ($d_{x^2-y^2}/d_{xy}$) states. Therefore, based on ligand field arguments, the Nb d^1 electron should occupy a state of d_{z^2} symmetry. Accordingly, it is common within the literature to see reference to a lower d_{z^2} subband when discussing the Nb-derived bands in proximity of the Fermi level [40]. This label persists despite the fact that DFT calculations show the lower energy state to have exclusively d_{z^2} character at the center (Γ) and $d_{x^2-y^2}/d_{xy}$ at the corners (K) of the BZ [45].

The electronic structure of NbSe$_2$ has been investigated with de Haas van Alphen (dHvA) oscillations [46] and ARPES experiments [47–49]. These studies revealed the presence of a small, flat Se-derived hole pocket centered at the Γ point [46,49] and two Nb-derived, cylindrical hole pockets at the Γ and K points [47–49]. A much larger mass enhancement was found for the Nb-derived bands as compared to the Se-derived bands, suggesting a stronger electron-phonon coupling [46]. For the $2H$ poly-type, each band is actually doubled, since each unit cell contains two formula units [41]. Based on the result of both dHvA and ARPES experiments, the Se-derived bands were found to be degenerate [46,49], while ARPES experiments revealed that the Nb-derived bands are in fact split, with the hole pockets at both the Γ and K points appearing as two distinct sheets, [47–49]. This splitting is, in general, resolvable in both energy and the momentum within ARPES data and is commonly referred to as bilayer splitting. In $2H$-NbSe$_2$ the mechanisms responsible for bilayer splitting are considered to arise from interlayer coupling and/or SOI [47,48].

Turning now to the effect of intercalation in TMDCs, the general interpretation is that the added electronic charge introduced by the intercalant changes the total number of carriers, without altering the local bonding of the host material [40]. Consequently, it is believed that intercalation does not change the Fermi surface (FS) and band topology of the host TMDC, as its only effect is to raise the chemical potential by an amount dependent upon the oxidation state of the intercalant [50]. Accordingly, Hall measurements for intercalated $2H$-NbS$_2$ were typically interpreted in terms of a filling in the lower d_{z^2} subband [51].

Applying arguments based on a rigid band picture to Cr$_{1/3}$NbS$_2$ would lead to the prediction that this material is semiconducting, having a completely filled d_{z^2} subband resulting from each Cr atom donating a full electron, i.e., half an electron per NbS$_2$ layer [44]. In light of recent findings, this simple picture is clearly untenable. While it is true that the carrier concentration for this material is low ($\sim 10^{20}$ cm^{-3})

[29] and that its resistivity is approximately three orders of magnitude larger than that of conventional metals, Cr$_{1/3}$NbS$_2$ is metallic and experiences a nearly tenfold drop in the resistivity occurring at the onset of magnetic order [29].

More recently, growing experimental evidence has begun to call the rigid band model into question. Most notably, several studies have shown that intercalation can alter the electronic properties of the host TMDC in nontrivial ways [38,52–54]. Two prominent examples include Cs and Rb intercalation of TaS$_2$ and TaSe$_2$, respectively [38,52,53]. Here, intercalating with alkali atoms had dramatically changed the charge density wave periodicity and induced a metal-to-semiconductor transition [38,52,53]. Moreover, an ARPES investigation directly comparing the electronic structure of NbSe$_2$, Mn$_{1/3}$NbS$_2$ and Ni$_{1/3}$NbS$_2$ has indicated that the added electronic charge introduced by the intercalant gives rise to a nonuniform doping across the FS [54]. For this reason, we present a detailed paper aimed at elucidating how Cr intercalation modifies the electronic structure of NbS$_2$.

III. EXPERIMENTAL DETAILS AND METHODS

The Cr$_{1/3}$NbS$_2$ single crystals were grown by chemical vapor transport using iodine as a transport agent [29]. Energy dispersive spectroscopy and x-ray diffraction measurements confirmed the stoichiometry and a $P6_322$ crystallographic space group.

The samples were cleaved *in situ* in ultrahigh vacuum, at different temperatures and base pressures, as described below. The exposed surfaces were always found to be shiny and flat, yielding sharp low energy electron diffractions (LEED) spots. The LEED patterns were found to be independent of the cleave temperature and robust against temperature cycling. Systematic temperature- and beam energy-dependent LEED measurements were performed using an Omicron SpectaLEED equipped with a W/Th filament and a viewing angle of 102°. In these LEED studies, samples were cleaved *in situ* at $T = 77$ K in a pressure better than 1×10^{-10} Torr.

For ARPES, Cr$_{1/3}$NbS$_2$ single crystals were cleaved *in situ* in a base pressure better than 4×10^{-11} Torr. Polarization dependent ARPES data were collected at Beamline 10.0.1 of the Advanced Light Source (ALS), using a Scienta R4000 electron energy analyzer, with the detector slit contained in scattering plane, i.e., the plane defined by the direction of the incoming photons and the direction of outgoing photoelectrons. The total instrumental energy resolution was 15 meV, while the angular resolution was set to $\pm 0.5°$, which corresponds to a momentum resolution of ≈ 0.06 Å^{-1} for the energies used in this experiment ($h\nu = 40$ and 48 eV). Additional ARPES data were collected at the Advanced Photoelectric Effect Experiment (APE) Beamline of the Elettra Synchrotron Facility using a Scienta DA30 electron energy analyzer operated in deflection mode, with the analyzer slit perpendicular to the scattering plane. All ARPES measurements were performed at $T < 20$ K.

Soft x-ray ARPES, core level PES, x-ray absorption (XAS), and resonant PES (ResPES) experiments were performed at the beamline for advanced dichroism (BACH) of the Elettra Synchrotron Facility. In these experiments, the samples were cleaved at $T = 300$ K in a pressure better than 1×10^{-9} Torr,

transferred to the analysis chamber ($P < 4 \times 10^{-10}$ Torr), and then measured at 77 K. Surface cleanliness was repeatedly confirmed by the absence of signatures related to oxidation in the Nb 3d core level spectra. The XAS measurements were performed in total electron yield by measuring the drain current through the sample using a picoammeter. Photoelectrons were measured with a Scienta R3000 electron energy analyzer. The PES and ResPES spectra were measured at normal emission with an energy resolution better than 0.3 eV. The SX-ARPES spectra were collected using the angular 21° mode, with the analyzer slit oriented perpendicular to the scattering plane. The energy resolution varied between 50 to 250 meV, while the angular resolution was $\Delta\theta = \pm0.75°$, resulting in a corresponding momentum resolution ranging from 0.2 to 0.37 Å^{-1} for the photon energy range used (196–736 eV). Additional PES measurements were performed on the high-energy branch of the APE beamline using an Omicron EA125 electron energy analyzer.

IV. RESULTS AND DISCUSSION

A. Surface characterization of Cr$_{1/3}$NbS$_2$

Before we present our extensive study of the electronic structure of Cr$_{1/3}$NbS$_2$, we address first whether the surface of Cr$_{1/3}$NbS$_2$ is representative of the bulk. This is especially relevant to understand how intercalation modifies the electronic structure of TMDCs when using surface sensitive measurements, such as ARPES. In general, it cannot be assumed that a surface cleaved *in situ* is representative of the bulk. This is particularly true for intercalated TMDCs. In these materials, the Cr intercalant atoms are positioned within the van der Waal gaps, where weakest bonding occurs. Not all of the Cr atoms are likely to remain bonded to an exposed freshly cleaved surface. Since the Cr layers are sandwiched between identical NbS$_2$ layers, half of the Cr atoms are likely to remain on the surface, and the other half is removed by the cleave. The distribution of Cr atoms on the top NbS$_2$ layer can, thus, be disordered.

The S 2p and Cr 2p core level PES spectra are shown in Fig. 1. The S 2p spectrum [Fig. 1(a)] consists of three main structures, indicating the presence of more than one component. The spectrum is fit very well with one pair of doublets. Each doublet accounts for the spin-orbit separation of the 2$p_{1/2}$ and 2$p_{3/2}$ core levels. Both the energy separation and the relative intensities of the two peaks in each doublet were constrained to be the same in the fit. The presence of two doublets cannot be attributed to inequivalent S sites in the bulk, since all S atoms lie in the same crystallographic site. Rather, the data indicate that the presence of the two doublets originates from S atoms located in the bulk, and on the surface. The difference between the binding energies (BE) of the two doublets is not small ($\approx$1 eV). This suggests that that bulk and surface S atoms have a different chemical environment. Specifically, the doublet at higher BE originates from S atoms bonded to the Cr intercalant atoms, while the doublet at lower BE originates from surface S atoms having a lower coordination as compared to the bulk, due to the absence of a fraction of Cr atoms on the surface. The Cr-bonded S atoms are expected to contribute to the majority of the signal, given
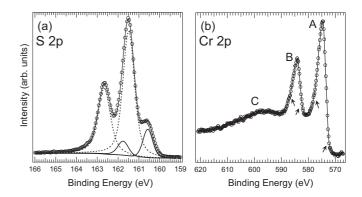

FIG. 1. (a) S 2p core level spectrum taken at normal emission from *in situ* cleaved Cr$_{1/3}$NbS$_2$ with $h\nu = 918$ eV. The BE separation between the doublet originating from the surface (solid line) and the deeper layers (dashed line) amounts to $\sim$1 eV. (b) Cr 2p core level recorded at normal emission with $h\nu = 918$ eV. Key features include a spin-orbit split doublet (A and B) and a loss feature (C). The arrows indicate kinks in the line shape of features A and B.

that the S 2p spectrum was taken at normal emission and is thus less surface sensitive. This is consistent with the fact that the doublet at higher BE is more intense than the lower BE doublet. A similar assignment for the components of the S 2p spectrum has been reported for Fe$_x$NbS$_2$ [55].

Our assignment of the structures in the S 2p spectrum thus suggests that in our experiment, the cleaved surface of Cr$_{1/3}$NbS$_2$ possesses a fraction of Cr atoms as compared to the bulk. Moreover, it is expected that the Cr core level spectra would exhibit a lower BE component originating from Cr atoms on the surface, which have a lower coordination than those in the bulk. The Cr 2p core level spectrum, shown in Fig. 1(b), does not show a clear indication of a lower BE surface component, despite the fact that it is more surface sensitive than the S 2p spectrum, since both spectra were recorded with the same photon energy. The spectrum consists of three main peaks, labeled as A, B, and C in Fig. 1(b). Peak C is a loss feature, and is observed in all of the other core level spectra measured in this paper. Its value, 24 eV, is consistent with the value assigned to a plasmon loss in Fe$_x$NbS$_2$ [55]. Peaks A and B correspond to the spin-orbit splitting of the Cr 2p core level. Both peaks are intrinsically broad. On the one hand, it is expected that the Cr 2p peaks have an intrinsic large width, consistent with a shorter core hole lifetime of the Cr 2p core level, as compared to the shallower S 2p core level. On the other hand, peaks A and B consist of more than one component, as evidenced in some kinks in their line shape [cf. Fig. 1(b)]. The kinks in the line shape on the low BE side of each peak are consistent with the presence of a surface component, which possibly indicates surface Cr to have a lower valence as compared to bulk [56], but a definite assignment remains inconclusive. We did not attempt to fit the Cr 2p spectrum due to its complicated nature.

The absence of a fraction of the Cr atoms from the surface after the cleave is consistent with the results of scanning tunneling microscopy (STM) experiments (Fig. 2). The STM image shown in Fig. 2(a) reveals two distinct surfaces types. While some locations on the terraces are atomically flat, most of the areas have a much higher corrugation. We refer to these
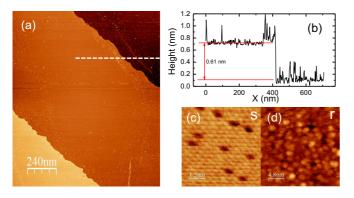
FIG. 2. (a) The STM image of *in situ* cleaved $Cr_{1/3}NbS_2$ single crystals taken with a bias voltage of -0.4 V illustrating the large-scale surface morphology. (b) Line profile along the broken line in (a) reveals a terrace step height of 0.61 nm with high corrugation near the step edge. (c) and (d) Atomic resolution images of the (c) "smooth" and (d) "rough" areas denoted by s and r, respectively.
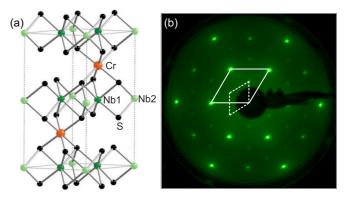

FIG. 3. (a) Unit cell of $Cr_{1/3}NbS_2$ taken from [29]. (b) Representative LEED image obtained from $Cr_{1/3}NbS_2$ with an electron beam energy of 215 eV. The unit cell of the 1×1 (solid) and $(\sqrt{3}\times\sqrt{3})R30°$ (dotted) reciprocal lattice are indicated.

two type of terraces as smooth and rough areas, respectively. The difference in corrugation between two distinct areas is best illustrated by the line profile corresponding to the dashed line in Fig. 2(a). The line profile [Fig. 2(b)] shows a terrace step height of 0.61 nm, with lower corrugation at its left (smooth area), and higher corrugation at its right (rough area). Based on the crystallographic lattice parameters of this material [29], such a step height is consistent with the separation distance between the NbS_2 planes. While the rough and smooth areas share the same base line, spikes of several angstroms can be seen in the rough area. Atomic scale images of the two areas are shown in Figs. 2(c) and 2(d). The hexagonal period in the atomic resolution image of the smooth area is around 0.566 nm [Fig. 2(c)]. This value is consistent with the unit cell dimension of bulk $Cr_{1/3}NbS_2$, where Cr atoms are ordered in a superstructure of dimensions $(\sqrt{3}a \times \sqrt{3}a)$, as compared to NbS_2. In contrast, the atomic resolution image of the rough area does not show any periodic order [Fig. 2(d)]. Despite the fact that the ordered intercalated Cr atoms are located in the Van der Waals gap below the surface NbS_2 plane, their ordering can produce a superstructure contrast in STM images of the surface through charge transfer modification of the local density of states (DOS) [57]. The atomic resolution image of the rough area does not show any periodic order [Fig. 2(d)]. Hence, we identify the rough areas as comprised of disordered residual Cr atoms that were left on the surface following the cleave, while the smooth areas are Cr free S terminated planes, leaving the surface, on average, Cr deficient as compared to the completely filled $(\sqrt{3}\times\sqrt{3})R30°$Cr superlattice in the bulk.

These STM results are corroborated by the results of LEED data collected with a systematically varying electron beam energy. These data are consistent with the absence of a $(\sqrt{3}\times\sqrt{3})R30°$ superstructure of ordered Cr atoms on the surface. The LEED patterns recorded using a beam energy of 215 eV, Fig. 3, reveal intense spots corresponding to the 1×1 periodicity of the NbS_2 lattice. Also visible, although with weaker intensity, are spots arranged in the $(\sqrt{3}\times\sqrt{3})R30°$ superstructure of the periodicity of the Cr atoms in the bulk. The $(\sqrt{3}\times\sqrt{3})R30°$ superstructure spots have smaller reciprocal lattice vectors than the 1×1 spots of the NbS_2

lattice and should, with increasing beam energy, thus enter the field of view of the screen well before the 1×1 spots enter the field of view at a beam energy of 60 eV. We observe, however, that they are only visible with significant intensity at beam energies larger than 80 eV. This observation can be rationalized by recognizing that with increasing electron beam energies the probing depth of the LEED experiment is increased; at low beam energies the experiment is more surface sensitive, and only the 1×1 NbS_2 termination is observed, whereas at higher beam energies the electron beam diffracts off of structures deeper below the surface, such as the $(\sqrt{3}\times\sqrt{3})R30°$Cr superstructure present in the bulk. Hence, we conclude that the observed $(\sqrt{3}\times\sqrt{3})R30°$ superstructure is located below the surface plane.

Taken together, PES, STM, and LEED data indicate that that in our experiments the surface of $Cr_{1/3}NbS_2$ consists of ordered S terminated regions, covered in some areas by residual Cr atoms that are not periodically ordered. As such, the surface possesses a stoichiometry and an atomic ordering that is different from that found in the bulk. This must be taken into consideration when using a surface sensitive technique, such as ARPES, to accurately understand how Cr intercalation modifies the electronic structure of NbS_2.

Figure 4 shows ARPES data collected along the ΓM direction with a photon energy equal to $h\nu = 48$ eV and photon polarization parallel to the sample plane. Despite the presence of disordered areas on the surface, the ARPES data are of high quality and reveal the presence of dispersing bands. Specifically, as shown by the image plot [Fig. 4(a)], there are two dispersing bands, one for energies $\approx$2-2.5 eV below the Fermi level (E_F), and a holelike band in proximity of E_F. The image plot reveals also the presence of nondispersing states with approximate energies of 1.5, 1, 0.5, and 0.25 eV below E_F. Also shown in Fig. 4(b) are the energy distribution curves (EDC). The EDCs consist in a stack of spectra where electron counts are plotted for fixed momenta as a function of energy. The nondispersing states are particularly visible in the EDCs. In light of the PES, LEED, and STM data discussed above, these nondispersing states are likely to originate from the Cr atoms randomly distributed on the surface. Consistently, such states are found to show no dispersion with photon
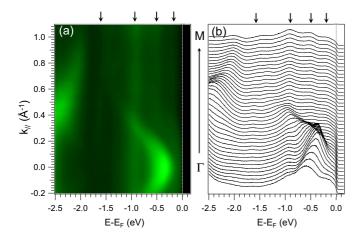
FIG. 4. High resolution ARPES spectra taken from $Cr_{1/3}NbS_2$ with σ-polarized photons of energy $h\nu = 48$ eV. Nondispersive surface states are indicated by arrows in both the (a) image plot and (b) stacked EDCs.

energy. Importantly, the presence of these nondispersive states is enhanced in these specific measuring conditions, namely, photon polarization in the sample plane, and photon energy $h\nu = 48$ eV, which close to the Cr $3p$ BE. In fact, these states are less visible when using photon energies nonresonating with the Cr $3p$ core level BE.

Further confirmation that the nondispersive states originate from Cr atoms is provided by the results of ResPES measurements. In a ResPES measurement, the incident photon energy is tuned across the absorption edge of a deeper core level of an atom. With this methodology, PES spectra of the valence band (VB) are element sensitive, since the portion of the VB spectrum associated with the resonating energy level(s) is enhanced, making it possible to identify the contribution originating from the selected element in the total VB structure. As shown in Figs. 5(b) and 5(c), there is a marked enhancement of states in the VB $\approx$1-2 eV below E_F when the photon energy is tuned across the Cr L edge, indicating that such states belong to the Cr $3d$ manifold. Notably, this enhancement was found using a photon polarization parallel to the sample plane, with photon energies tuned in proximity of the shoulder located on the low energy side of the XAS spectrum [Fig. 5(c)]. A similar shoulder is reported in the Fe L_3 XAS spectrum of Fe_xNbS_2, but no claim is made as to its origin [55]. Our results suggest that the low energy shoulder in the Cr XAS spectrum originates from nonperiodically ordered Cr on the surface, which may have a lower valence as compared to bulk [56]. Additionally, the absence of sharp multiplets in the XAS spectrum in Fig. 5(c) implies Cr to be in more of a metallic environment.

B. Soft x-ray ARPES in $Cr_{1/3}NbS_2$

Although the data shown in Fig. 4 are of high quality, it is still possible that conventional ARPES data are more representative of the surface, rather than the intrinsic electronic and band structure of bulk $Cr_{1/3}NbS_2$. To address whether conventional ARPES experiments can be used to study the bulk electronic structure of cleaved $Cr_{1/3}NbS_2$, ARPES data were collected for different photon energies ranging from 40 eV to
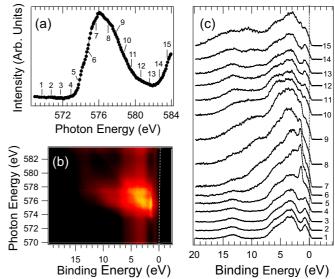

FIG. 5. The ResPES measured from $Cr_{1/3}NbS_2$ across the Cr L_3 absorption edge with photon polarization contained entirely in the sample plane. (a) Cr L_3 XAS measured in total electron yield. (b) ResPES image plot and (c) representative line profiles extracted at the corresponding photon energies labeled in (a).

the SX regime, with energies of several hundreds of electron volts, to directly compare data representative of different probing depths. Figure 6 shows a comparison between the image plots of ARPES data taken along the ΓK direction with conventional ($h\nu = 40$ eV; Fig. 6, a_1) and higher photon energies in the SX regime ($h\nu = 196, 401, 736$ eV in Fig. 6, a_2, a_3, and a_4, respectively). The estimated probing depths corresponding to the used SX photon energies are 23, 32, and 44 Å, to be compared with the 12.1 Å spacing of the unit cell along the c axis and the $\sim$5-7 Å probing depth of conventional ARPES.
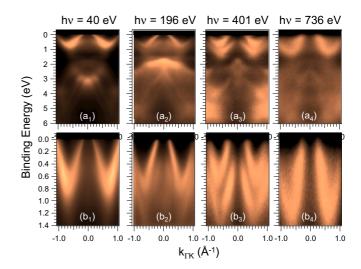

FIG. 6. ARPES spectra measured from $Cr_{1/3}NbS_2$ along the ΓK direction over a wide (a_1-a_4) and narrower (b_1-b_4) binding energy range using photon energies $h\nu = 40$ eV (a_1, b_1), $h\nu = 196$ eV (a_2, b_2), $h\nu = 401$ eV (a_3, b_3) and $h\nu = 736$ eV (a_4, b_4). Spectra at $h\nu = 40$ eV has been symmetrized with respect to the Γ point.

Before commenting further on the photon energy dependence of the data shown in Fig. 6, note that there are some technical aspects of SX-ARPES that differ from conventional ARPES measurements [58,59]. First, in SX-ARPES there is a substantial loss in the overall energy resolution of the experiment, since at higher photon energies, both the photon and the spectrometer resolution worsens. The spectrometer resolution is worse because of the necessity of using higher pass energies to compensate for the lower cross section of the states in proximity of E_F. Second, the photon momentum must be taken into account when performing the angle-to-k conversion of the data. Third, there is a significant worsening in momentum resolution when the photoelectron kinetic energy E_{KIN} is increased, since the momentum resolution scales as $(E_{KIN})^{1/2}$. Finally, as the photon energy increases, the photoelectron matrix elements are much less sensitive to variations of the in-plane crystal momentum [59].

In our experiments, the photon energies $h\nu = 196, 401$, and 736 eV were chosen so as to yield the same $k_z = 0$ value in the reduced zone scheme given an inner potential of 14 eV. For such photon energies, the overall energy resolution was ≈ 53, 139, and 250 meV, while the momentum resolution was ≈ 0.18, 0.27, and 0.36 $\text{\AA}^{-1}$, respectively. To a first approximation, the worsening of the energy and momentum resolution at higher photon energies manifest in the image plots as a smearing of the spectral features along the vertical and horizontal axis, respectively. Such smearing renders a comparison between the image plots not immediate. In addition, there is a small, but noticeable sample misalignment in the SX data. It is still possible to identify the same spectral features in the data for all photon energies such as, for example, the structure at $k_{\Gamma K} = 0$ located ≈ 2 eV below E_F and the bands within ≈ 1.5 eV of E_F. The intensity of these features changes for different photon energies. This is particularly evident for the bands in proximity of E_F, which are shown in more detail in Fig. 6, b_1-b_4. The data taken with $h\nu = 40$ eV (Fig. 6, a_1, b_1) and $h\nu = 196$ eV (Fig. 6, a_2, b_2) bear similarities concerning the approximate bandwidth, and the Fermi momenta k_F, i.e., the positions in momentum space where the bands cross E_F. More than one band contribute to the signal, as confirmed by an analysis of the MDCs and the EDCs, discussed in Fig. 7. The intensity of the lower lying band increases when the data are taken with $h\nu = 401$ eV (Fig. 6, a_3, b_3). At higher energy $h\nu = 736$ eV (Fig. 6, a_4, b_4), the loss of resolution produces a broadening of spectral features. The lower energy resolution has the effect of smearing the image particularly along the energy axis, giving the appearance of only a single broad band.

These observations are corroborated by an analysis of the MDCs and EDCs corresponding to the image plots in Fig. 6, b_1-b_4, shown in Fig. 7. Two bands are clearly seen in the EDCs for the data taken at $h\nu = 40$ eV (Fig. 7, a_1), $h\nu = 196$ eV (Fig. 7, a_2) and $h\nu = 401$ eV (Fig. 7, a_3). The contribution to the signal originating from the lower band increases when the photon energy is increased. The asymmetric line shape of the EDCs in Fig. 7, a_4 indicates that the signal originating from higher probing depth is comprised of the same bands observed at lower photon energies, although the worse momentum and energy resolution make it impossible to resolve the bands. From the data taken with $h\nu = 401$ eV (Fig. 7, a_3), the bottom of the lower band appears to be located ≈ 1.1 eV below E_F. The
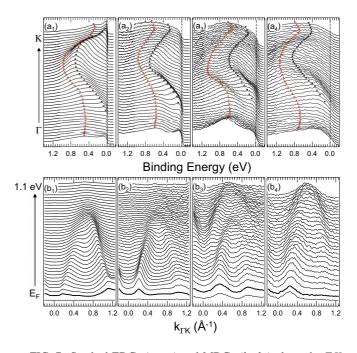

FIG. 7. Stacked EDCs (a_1-a_4) and MDCs (b_1-b_4) along the ΓK direction extracted from the corresponding image plots depicted in Fig. 6, b_1, b_4. Tick marks tracing the dispersion of the two bands in proximity to E_F have been added to the EDC stacks in a_1-a_4 as a guide to the eye. In the MDC stacks, the MDC at E_F is denoted with a thicker line.

contribution of this band is visible in the EDC stack of the data taken with $h\nu = 40$ eV (Fig. 7, a_1) only in proximity of the Γ and K points but not in-between. The presence of spectral weight located ≈ 1.1 eV below E_F is, however, visible from the corresponding MDC plot (Fig. 7, b_1). These observations suggest that the progressive increase of the contribution to the signal of the lower band for higher photon energies is due to matrix element effects, rather than being indicative of differences in the electronic structure corresponding to different sampling depths.

This is confirmed with further analysis of the data. The MDC curves at E_F, highlighted in Fig. 7(b), are shown for comparison in Fig. 8. The spectra are shown for the region in proximity to the Γ point, as the abovementioned sample misalignment does not allow to observe clearly the Fermi crossing at the K point. In this plot, peaks in the curves identify the positions of the Fermi momenta k_F. Three main structures, labeled as α, β_1, and β_2, can be identified in the low energy data ($h\nu = 40$ eV). The curves become much broader for higher photon energies, consistent with the worsening of momentum resolution. Taking the latter into account, the data taken with $h\nu = 196$ eV are in good agreement with the $h\nu = 40$ eV data as far as structures α and β_1 are concerned. On the contrary, structure β_2 is not visible. Its presence is, however, fully consistent with the data taken with $h\nu = 401$ eV. The intensity at the momentum corresponding to structure β_2 is substantial, comparable to that of structures α and β_1 and cannot be accounted for by a broadening of the data taken with $h\nu = 196$ eV. The intensity of the data taken with $h\nu = 736$ eV is higher at the momentum corresponding
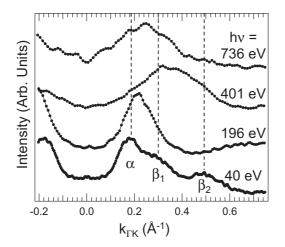
FIG. 8. Direct comparison of MDCs extracted at E_F for $h\nu = 40$, 196, 401, and 736 eV depicting k_F crossings about Γ. Features from the $h\nu = 40$ eV spectra are labeled α, β_1, and β_2 for the purpose of comparisons. For a description of this notation, see text.

FIG. 9. Comparison of (a) valence band and (b) Nb $3d$ PES spectra for NbS_2 (top) and $Cr_{1/3}NbS_2$ (bottom) as measured at normal emission with $h\nu = 750$ eV. From (a), a comparison of similar features in the VB as well as the shallow $S\,3s$ core level demonstrates a 0.4 eV shift towards higher binding energy. The suppression of the higher BE peaks of the Nb $3d$ doublet (solid line) observed in $Cr_{1/3}NbS_2$ is visible in (b).

to structures α and β_1, while the intensity in at β_2 is now suppressed. The weight in the different curves of structures α, β_1, and β_2 does not vary monotonically with increasing the photon energy. This is not consistent with the notion that the differences in the data corresponding to different photon energies are a manifestation of a variation of the electronic structure as a function of probing depth. Rather, the photon energy dependence of the MDCs at E_F is more easily explained as a result of matrix element effects.

In light of these observations, the differences between the data taken at different photon energies are more easily explained as a result of the variation of the matrix elements, rather than suggesting intrinsic major differences of the electronic structures representative of different depths. Taking into consideration the intrinsic limitations of SX-ARPES in the determination of the Fermi momenta and dispersion of the bands as a result of lower energy and momentum resolution, there is consistency between data representative of different probing depths. This means that despite the surface of $Cr_{1/3}NbS_2$ being Cr deficient and partially disordered, salient features of the electronic structure revealed by low energy ARPES, such as bands dispersion and Fermi momenta, are not significantly modified as compared to the bulk.

C. Direct comparison of ARPES data in NbS_2 and $Cr_{1/3}NbS_2$

The common interpretation used in describing the modification of the electronic structure for a host TMDC upon atomic intercalation is that of a rigid band picture [40,50]. The layer formed by the intercalant atoms act as a charge reservoir donating electronic charge, with the effect of raising the chemical potential without altering the overall FS and band topology of the host material. To investigate the validity of this interpretation for $Cr_{1/3}NbS_2$, we directly compared the results of core level PES and ARPES measurements in NbS_2 and $Cr_{1/3}NbS_2$.

The integrated VB, $S\,3s$, and Nb $3d$ PES core level spectra are shown in Fig. 9. The VB exhibits three main structures, which in $Cr_{1/3}NbS_2$ are shifted by ≈ 0.4 eV to higher BE
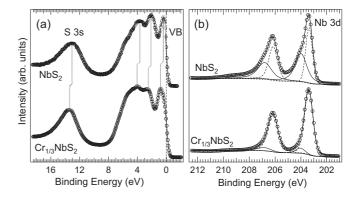
as compared to NbS_2. The same shift occurs between the $S\,3s$ shallow core level spectra [Fig. 9(a)]. This observation suggests that the chemical potential is increased in NbS_2 upon intercalation of Cr atoms, consistent with the notion that in $Cr_{1/3}NbS_2$ Cr atoms donate electrons to the NbS_2 layers. The Nb $3d$ core level spectra do not appear to be shifted with respect to one another [Fig. 9(b)]. Notably, the line shape of the spectra is different. Two spectral components are present in the spectrum of NbS_2. In the spectrum of $Cr_{1/3}NbS_2$, the component at higher BE is strongly suppressed. Given the higher BE component observed the Nb $3d$ spectrum to be absent from the Nb $3p$ core level, we exclude the possibility that this component arises due to oxidation or contamination. Rather, the difference in the line shapes indicates that Cr intercalation alters the local electronic environment of the Nb atoms. In agreement with the conclusions reported in similar studies on Fe_xNbS_2 [55], the two components in the spectra are indicative of different screening channels. The component at lower and higher BE are identified with the so-called well-screened, and poorly screened peak, respectively. The suppression of the poorly screened satellite in favor of the well-screened main peak in $Cr_{1/3}NbS_2$ is consistent with the fact that charge donation, resulting from Cr intercalation, increases the screening charge in the NbS_2 layers.

The FS of NbS_2 and $Cr_{1/3}NbS_2$ are shown for comparison in Fig. 10. Two hole pockets are observed at Γ and K. The size of both pockets is reduced in $Cr_{1/3}NbS_2$ as compared to NbS_2, consistent with the fact that Cr intercalated atoms donate electrons to the NbS_2 layers. It is also evident, however, that in $Cr_{1/3}NbS_2$ the structure at the Γ point is more complex as compared to NbS_2. This suggests that Cr intercalation plays a more complex role than just injecting carriers into the NbS_2 layers, possibly impacting significantly the electronic structure and FS topology of NbS_2.

Figure 11 shows the image plots corresponding to cuts along the ΓK direction for both linear vertical (LV) and linear horizontal (LH) photon polarizations. The photon polarization is contained entirely in the sample plane for LV, while for
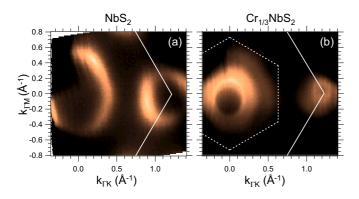
FIG. 10. The FSs of (a) NbS_2 and (b) $Cr_{1/3}NbS_2$ measured along the ΓK direction using photons of energy $h\nu = 40$ eV. The solid and broken lines indicate the 1×1 and $\sqrt{3} \times \sqrt{3}$ BZ, respectively.

LH the polarization has both a parallel and perpendicular component to the sample plane. These data, taken with a photon energy $h\nu = 40$ eV, are representative of the zone center along the k_z direction. The difference of the band structure in NbS_2 and $Cr_{1/3}NbS_2$ appears to be consistent with a ≈ 0.4 eV shift of the spectral features as measured over a large energy range, as particularly evidenced for the data taken in
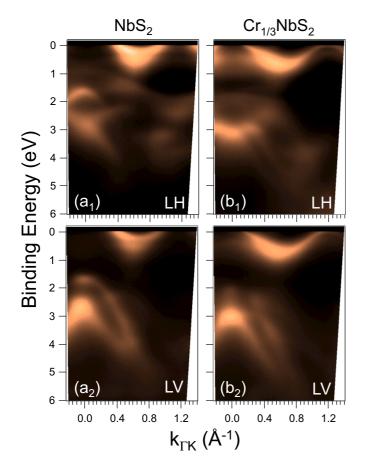

FIG. 11. Band dispersion of (a_1, a_2) NbS_2 and (b_1, b_2) $Cr_{1/3}NbS_2$ measured along the ΓK direction over a wide BE range using $h\nu = 40$ eV photons having a polarization horizontal (a_1, b_1) or vertical (a_2, b_2) with respect to the scattering plane.
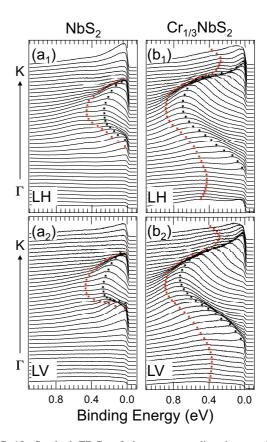

FIG. 12. Stacked EDCs of the corresponding image plots in Fig. 11 shown within ~ 1 eV from E_F. Tick marks tracing the dispersion of the bonding (red) and antibonding (black) bilayer split Nb-bands have been added as a guide to the eye. The Nb-derived bonding band is found to sink ~ 200 meV below E_F (b).

LV polarization (Fig. 11, b_2). The magnitude of this shift is the same as found for the shallow S $3s$ core level [cf. Fig. 9(a)]. The same conclusions are drawn from inspection of the same cuts taken with photon energy $h\nu = 48$ eV, with the data being representative of the zone edge along the vertical direction.

Band structure calculations for bulk NbS_2 are expected to provide guidance for establishing a firm comparison between NbS_2 and $Cr_{1/3}NbS_2$. According to the calculations for NbS_2, three bands cross E_F in proximity of the Γ point and two bands at the K point [60]. An analysis of the EDC (Fig. 12) and MDC (Fig. 13) stacks reveals that in NbS_2 two bands cross E_F at both the Γ and K points. We identify these two bands with the bilayer split Nb $4d$ bands. The chalcogen p_z band that crosses E_F closer to the Γ point, as predicted by the calculations, is not visible within ≈ 1.5 eV below E_F, unlike in the related compound $NbSe_2$ [49].

A comparison of the stacked EDCs in proximity to E_F likewise shows a similarity of the salient features of the NbS_2 and $Cr_{1/3}NbS_2$ band structure (Fig. 12). In $Cr_{1/3}NbS_2$, two bands can be easily traced. The upper band is found to have a well-defined Fermi crossing in the vicinity of the Γ and K points, while the lower band sinks to ≈ 0.2 eV below E_F. In a rigid band interpretation, this can be understood in terms of a filling of the lower bilayer split-Nb $4d$ band, i.e., the bonding band, due to the added carriers introduced by Cr intercalation, resulting in an increase of the chemical potential.
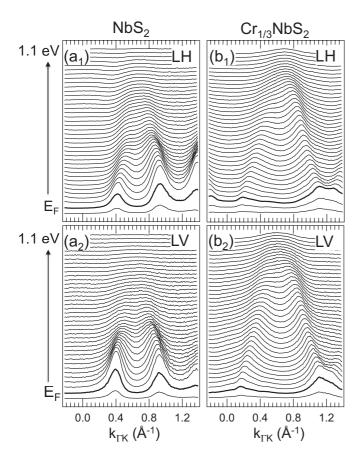
FIG. 13. Stacked MDCs of the corresponding image plots in Fig. 11 shown within ∼1 eV from E_F. The MDC at E_F is denoted with a thicker line.
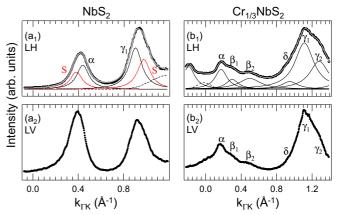

FIG. 14. Direct comparison of MDCs at E_F extracted from the data shown in Fig. 13. In the fit of the MDCs, shown in (a_1) and (b_1), the broken lines denote spectral weight originating from the background. The main features of the MDCs in $Cr_{1/3}NbS_2$ (b_1 and b_2) are likewise denoted in NbS_2 (a_1). In (a_1), peak S (red) sinks below E_F in $Cr_{1/3}NbS_2$. A slight misalignment of the sample is responsible for an asymmetry with respect to Γ of the MDCs in (a_2) and (b_2).

The MDC stacks for NbS_2 and $Cr_{1/3}NbS_2$, compared in Fig. 13, indicate that data taken with both polarizations for each compound appear to be very similar, as also shown by a direct comparison of the MDC at E_F (Fig. 14). For NbS_2, the MDC stacks clearly show that two bands cross E_F, at both the Γ and the K point. The use of two distinct peaks to fit the MDCs at E_F at both Γ and K fits the data well (Fig. 14, a_1).

In the case of $Cr_{1/3}NbS_2$, for both the bands at Γ and K, understanding how Cr intercalation impacts the band structure of NbS_2 is in fact not trivial. The MDC at E_F reveal three clearly identifiable structures near Γ, and a broad structure at K (Fig. 14, b_1, b_2). The presence of the three structures in proximity of the Γ point indicates that three bands cross E_F near the zone center, denoted hereafter as α, β_1, and β_2. Since Cr intercalation has the effect of raising the chemical potential, the NbS_2-derived bands at Γ should cross E_F at a lower k_F than in NbS_2. The MDC at E_F indicates that the α and β_1 bands have a lower k_F than in NbS_2. On the contrary, the k_F of the β_2 band (0.5 Å^{-1}) is greater than in NbS_2. This observation indicates that this band does not originate from the band structure of NbS_2 as a result of an increased chemical potential. The same conclusion is reached regarding the β_1 band. Although both the α and β_1 bands cross E_F closer to the Γ point than in NbS_2, only one band can originate from the band structure of NbS_2. Indeed, only one of the two NbS_2-derived bands crosses

E_F, while the other one sinks below E_F, as indicated by the presence of a band below E_F, which is not present in NbS_2, in the image plot (cf. Fig. 11) and the EDCs (cf. Fig. 12). Based on an inspection of the DFT calculation for NbS_2, a shift of the chemical potential compatible with our observations would result in a shift of k_F of the antibonding band consistent with the position of the α band in $Cr_{1/3}NbS_2$. Therefore, in $Cr_{1/3}NbS_2$, the β_1 and β_2 bands crossing E_F in proximity of the Γ point are not simply NbS_2 derived. Given that the data were taken at a temperature lower than the magnetic transition temperature T_C, it is possible that two such bands derive from a single exchange-split band.

In $Cr_{1/3}NbS_2$ the MDC at E_F reveals a broad structure in proximity of the K point. The large intrinsic width of this structure is consistent with the fact that the sets of bands around the K point approach each other due to the shift of the chemical potential. A fit of the MDC in proximity of the K point reveals two peaks, labeled γ_1 and γ_2, which are symmetrically located with respect to the K point. We identify the position of these peaks as the k_F of one of the two set of bands that are also visible in NbS_2 [Fig. 14(a)]. Consistently, the k_F of the γ_1 band in $Cr_{1/3}NbS_2$ is greater than in NbS_2. A third band denoted as δ crosses E_F at $\approx 0.95 \text{ Å}^{-1}$. Since the lower band in NbS_2 has been observed to sink below E_F upon Cr atoms intercalation (cf. Fig. 12), the δ band is not NbS_2 derived.

On the basis of the data presented so far, we conclude that, despite the similarity of the salient features of the NbS_2 band structure, the electronic structure of $Cr_{1/3}NbS_2$ is not consistent with the notion of a simple rigid band picture. In particular, Cr intercalation does modify the electronic structure of NbS_2 by adding two additional bands at $\Gamma(\beta_{1,2})$ and one additional band at $K(\delta)$.

D. Polarization-dependent ARPES data in $Cr_{1/3}NbS_2$

Further validation of concluding statements in the previous subsection and additional important insights are revealed
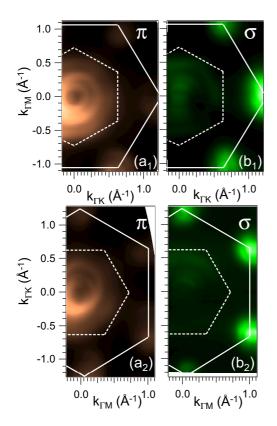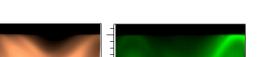
FIG. 15. The FSs of $Cr_{1/3}NbS_2$ measured along the (a_1 and b_1) ΓK and (a_2 and b_2) ΓM direction using π-polarized (a_1 and a_2) and σ-polarized (b_1 and b_2) photons of energy $h\nu = 40$ eV. Solid and broken lines denote the 1×1 and $\sqrt{3} \times \sqrt{3}$ BZ, respectively.

by polarization dependent ARPES data collected in π and σ geometry, where the photon polarization is parallel and perpendicular to the scattering plane, respectively. In this set of experiments, the scattering plane is oriented perpendicular to the sample surface and coincides with the mirror plane of the sample.

In $Cr_{1/3}NbS_2$, the bands forming the FS derive from the d orbitals of Nb and Cr. Polarization dependent ARPES allows the determination of the majority orbital character of each band in $Cr_{1/3}NbS_2$, which can be identified from the symmetry of the photoelectron's initial state [61,62]. The intensity in ARPES experiments is modulated by a dipole matrix element, i.e., the triple product of the dipole operator and the initial and final state photoelectron wave functions. When the detector slit is contained in the mirror plane, the final state of the photoelectron wave function is of even parity (with respect to the mirror plane). Consequently, a photoelectron can be detected only if the product of the dipole operator and the initial state wave function is of even parity. Since the dipole operator is even (odd) for π (σ) polarization, σ- and π-polarization geometries are sensitive to initial state photoelectron wave functions of odd and even parity, respectively.

The FS of $Cr_{1/3}NbS_2$ measured with the analyzer slit oriented along the ΓK and ΓM directions in both σ- and π-polarization geometries is shown in Fig. 15. The intensity of the features at Γ and K depends sensitively on the photon polarization. The intensity of the bands crossing E_F close to the
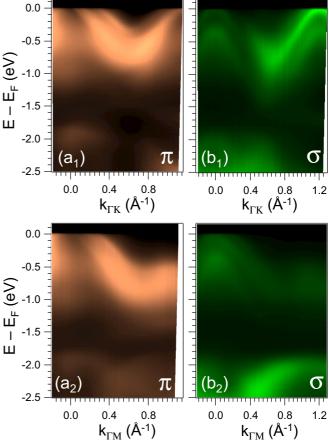

FIG. 16. Band dispersion measured along the (a_1 and b_1) ΓK and (a_2 and b_2) ΓM direction using π-polarized (a_1 and a_2) and σ-polarized (b_1 and b_2) photons of energy $h\nu = 40$ eV.

Γ point is markedly enhanced in π polarization. This clearly indicates that these bands have an even orbital character. The intensity of these bands does not change appreciably when the mirror plane is oriented along the ΓK or ΓM directions, suggesting that these bands have an out-of-plane orbital character. To the contrary, the use of σ polarization enhances the intensity of the bands crossing E_F in proximity of the K point, indicating that these bands have an odd orbital character. The symmetry of the states at K cannot be unambiguously determined since for cuts along the ΓM directions the K point is not contained in the mirror plane. Our results are consistent with *ab initio* DFT calculations for $2H$-NbSe$_2$, which identify the orbital character at Γ to be chalcogen p_z and Nb d_{z^2} derived and Nb $d_{xy}/d_{x^2-y^2}$ at K [45]. Importantly, in $Cr_{1/3}NbS_2$ the $\beta_{1,2}$ and δ bands, absent in NbS$_2$, have thus predominant out-of-plane (d$_{z^2}$) and in-plane character ($d_{xy}/d_{x^2-y^2}$), respectively.

More information is provided by specific cuts taken along the ΓK and ΓM directions with π and σ polarization. Image plots of the data taken with photon energies of 40 eV and 48 eV are shown in Figs. 16 and 20, with the corresponding EDC and MDC stacks in Figs. 17 and 18, and Figs. 21 and 22, respectively. The data taken in σ polarization reveal a holelike band of weak intensity, with its maximum that crosses E_F close to the Γ point. This band, visible in both the cuts along ΓK
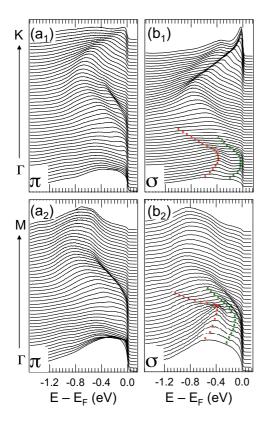
FIG. 17. Stacked EDCs of the corresponding image plots in Fig. 16 shown within $\sim$1 eV from E_F. Tick marks tracing the dispersion of the backfolded band (green) and Nb-derived bonding band (red) in (b_1) and (b_2) have been added as a guide to the eye.

and ΓM, can be traced only $\approx$200 meV below E_F, as shown by the MDCs (Fig. 18). This band is not visible in data taken with a photon energy of $h\nu = 48$ eV. There is no trace of such band in π polarization, and even in σ polarization its intensity is very weak. These considerations lead us to believe that this is not a new band visible only for particular experimental conditions. Rather, on the basis of an analysis shown in Fig. 19, we identify this band as a replica at the Γ point of the bands found at the K point. Given the commensurate $(\sqrt{3}\times\sqrt{3})R30°$ superstructure of the Cr atoms, the Γ and K points of the 1×1 (NbS$_2$) BZ are separated by a reciprocal lattice vector of the BZ of the $(\sqrt{3}\times\sqrt{3})$ superstructure [Fig. 19(a)]. It is, thus, expected that the bands at K fold back to the Γ point, while replicas of the states at Γ should be found at K. When bands have opposite character, i.e., hole- and electronlike, the identification of band backfolding is usually facilitated by the possibility of observing band-gap openings resulting from avoided level crossings [63]. In our case, given that both the bands at Γ and K are holelike, the identification of weak, backfolded bands is more challenging.

The signature of the presence of back-folded bands at Γ is, however, indicated by the correspondence of the bands at Γ and the trace of the MDC peak positions of the most prominent band at K translated by the reciprocal lattice vector of the BZ of the $(\sqrt{3}\times\sqrt{3})$ superstructure [Figs. 19(b) and 19(c)]. The same correspondence can be qualitatively observed in the image plot for data taken with photons of energy $h\nu = 196$ eV and polarization parallel to the sample plane [Fig. 19(d)]. The fact
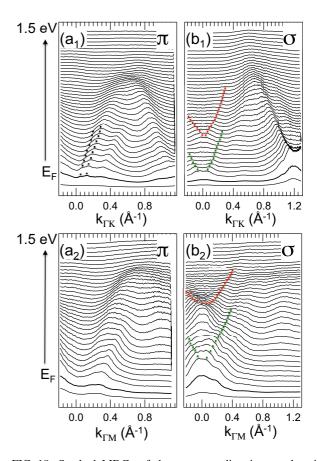

FIG. 18. Stacked MDCs of the corresponding image plots in Fig. 16 shown within $\sim$1 eV from E_F. The MDC at E_F are denoted with the thicker line. Tick marks tracing the dispersion of the backfolded band (green) and Nb-derived bonding band (red) in (b_1) and (b_2) have been added as a guide to the eye. Additional tick marks tracing the dispersion of the split α band (black) have been added in (a_1) as a guide to the eye.

that such bands at Γ are clearly observed when the polarization is parallel to the sample plane is consistent with their origin as backfolded bands, since the latter are expected to retain the same, i.e., in-plane, orbital character as the states at K. The importance of backfolding and replicas stems from the fact that such features are a consequence of Cr ordering. The presence of backfolded bands at Γ revealed by data taken with different photon energies indicates that although cleaved surfaces of Cr$_{1/3}$NbS$_2$ have nonperiodic and nonstoichiometric Cr ordering, conventional ARPES data reveal the presence of the $(\sqrt{3}\times\sqrt{3})R30°$ superstructure due to Cr atoms as in the bulk.

Another interesting feature revealed by the data taken in σ polarization is the accentuated contribution to the spectra of the "bonding" band $\approx$0.2 eV below E_F in proximity of the Γ point, as shown by both the image plot (Fig. 16, b_2) and the MDCs (Fig. 18, b_2). This is particularly evident in the image plots and EDC stacks of the data taken with photon energy $h\nu = 48$ eV, as shown in Figs. 20 and 21. Importantly, this photon energy coincides with the BE of the Cr 3p core level. The enhancement of the spectral weight of the bonding band for this particular energy thus indicates that Cr intercalation results in a filling of the Nb-derived bonding band, consistent
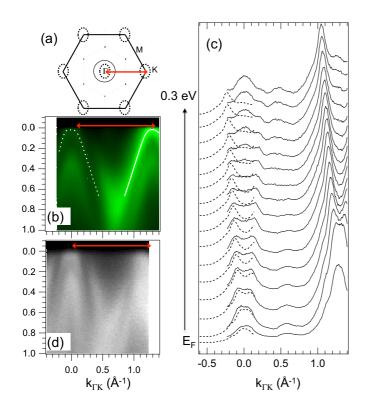
FIG. 19. (a) Sketch of the 1×1 BZ illustrating how the hole-like band at K folds due to a $\sqrt{3} \times \sqrt{3}$ superlattice potential. (b) Band dispersion taken along the ΓK direction with σ-polarized photons of $h\nu = 40$ eV. Superimposed on the image plot is a trace of the MDC peak positions of the band at K (solid) translated by a $\sqrt{3} \times \sqrt{3}$ lattice vector (broken line). (c) The MDC stacks having a negative offset taken from 300 meV to E_F from the image plot in (b). Broken lines have been translated by a $\sqrt{3} \times \sqrt{3}$ lattice vector and rescaled so as to directly compare the dispersion. (d) Band dispersion measured along the ΓK direction with LV polarized photons of energy $h\nu = 196$ eV.

FIG. 20. Band dispersion measured along the (a_1) and (b_1) ΓK and (a_2) and (b_2) ΓM direction using π-polarized (a_1) and (a_2) and σ-polarized (b_1) and (b_2) photons of energy $h\nu = 48$ eV.

with the occurrence of some hybridization between the Cr and Nb atoms. Since σ polarization was used, the data indicate that in Cr$_{1/3}$NbS$_2$ the bonding band has also a marked orbital character at the Γ point consistent with xy and/or x^2-y^2. This is in contrast to the exclusive d_{z^2} character at Γ as predicted by the results of DFT calculations of NbSe$_2$ [45]. In fact, in NbSe$_2$ the a_1' state (with symmetry d_{z^2}) is lower in energy than the two doubly degenerate e' states ($d_{x^2-y^2}/d_{xy}$) [40]. Qualitatively, this can be rationalized by invoking a ligand field model. Namely, for the distance between neighboring Nb atoms being larger along the c axis as compared to the ab plane, a smaller overlap of the Nb $4d$ orbitals along the c axis would lower the energy of the a_1' (d_{z^2}) states relative to the e' ($d_{x^2-y^2}/d_{xy}$) states. In Cr$_{1/3}$NbS$_2$, the presence of intercalated Cr atoms directly above and below the Nb atoms can act to raise the energy of the a_1' states relative to the e' states. This is a consequence of an increased overlap between the Nb $4d$ and Cr $3d$ orbitals along the c axis. While a quantitatively determination of the specific energy differences between the a_1' and e' states in NbS$_2$ and Cr$_{1/3}$NbS$_2$ would involve a Madelung calculation, on the basis of the data, this inversion seems possible. The $d_{x^2-y^2}/d_{xy}$ orbital character of the bonding
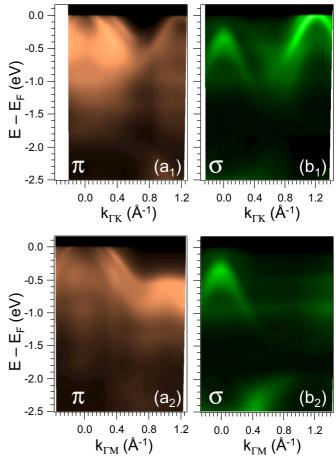
band is thus a further indication that a picture based on a rigid shift model is untenable for Cr$_{1/3}$NbS$_2$.

An inspection of the MDCs of the data taken with polarization-dependent ARPES reveal further details about the bands crossing E_F in Cr$_{1/3}$NbS$_2$. The NbS$_2$-derived α band was identified by a peak at $\approx 0.15 \, \text{Å}^{-1}$ in the data shown in Fig. 14, b_1, b_2). The MDCs of the data taken in π polarization, shown in Fig. 18, a_1, a_2) and Fig. 22, a_1, a_2), reveal that the α band is actually split. This is evident from the MDCs at E_F shown in Fig. 23(a), which shows how, particularly for the spectra measured along the ΓK direction, the α band is actually comprised of two structures labeled α_1 and α_2. The parallel dispersion can be traced for up to 150 meV below E_F, as shown in Fig. 18, a_1, a_2 and Fig. 22, a_1, a_2.

The MDCs at E_F of the data taken along the ΓK direction in σ polarization are shown in Fig. 23(b). The data reveal the presence of a structure at $\approx 1.05 \, \text{Å}^{-1}$, labeled δ_2. In addition, the spectrum taken at 40 eV exhibit an additional shoulder (δ_2) located at $\approx 0.9 \, \text{Å}^{-1}$, possibly present also in the data taken at 48 eV. Since according to the fit shown in Fig. 14, b_1 the Cr-derived δ band crosses E_F at $\approx 0.95 \, \text{Å}^{-1}$, the data suggest that the δ band could in fact be split into the two δ_1 and δ_2 bands.
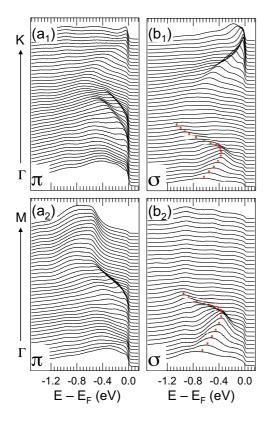
FIG. 21. Stacked EDCs of the corresponding image plots in Fig. 20 shown within ~1 eV from E_F. Tick marks tracing the dispersion of the Nb-derived bonding band (red) in (b_1) and (b_2) have been added as a guide to the eye.

On the basis of these data, it is only possible to speculate on the origin of the splitting of the α and δ bands. Importantly, while the α band is NbS_2 derived, the δ band is not, i.e., its existence cannot be accounted by the band structure of NbS_2. Similar to the $\beta_{1,2}$ bands, its origin stems from a modification of the NbS_2 electronic structure following Cr intercalation. Given that the splitting of the δ_1 and δ_2 bands is $\approx 0.15\,\text{Å}^{-1}$, not very different from the value $\approx 0.20\,\text{Å}^{-1}$ of the k_F for the β_1 and β_2 bands and that the data were taken at a temperature lower than T_C, it is plausible that the δ band is exchange-split band. An exchange mechanism, however, does not seem to be the origin of the splitting of the α band. Its splitting ($0.06\,\text{Å}^{-1}$) is much smaller than that of the β and δ bands. As the γ_1 band, the α band is NbS_2 derived. The γ_1 band does not exhibit any obvious splitting, suggesting that the only bands that are exchange split are Cr derived. The importance of SOI in $Cr_{1/3}NbS_2$ suggests that the splitting of the α band could be a signature of broken inversion symmetry. The SOI leads to a spin splitting of the energy bands when Kramer's degeneracy is broken. This occurs either when time reversal symmetry is broken, as in a ferromagnetic state, or inversion symmetry is broken. In the latter case, the consequential spin splitting of the bands is referred to as the Dresselhaus effect if the inversion symmetry is lifted in the bulk of the crystal or as the Rashba effect when inversion symmetry is broken because of the creation of a surface. Importantly, inversion symmetry in the bulk is broken in $Cr_{1/3}NbS_2$, but not in NbS_2,
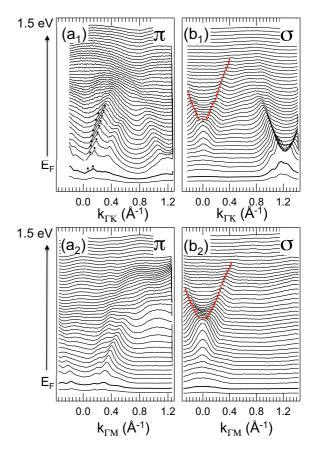

FIG. 22. Stacked MDCs of the corresponding image plots in Fig. 20 shown within ~1 eV from E_F. The MDC at E_F are denoted with a thicker line. Tick marks tracing the dispersion of the Nb-derived bonding band (red) in (b_1) and (b_2) and the split α band (black) in (a_1) have been added as a guide to the eye.
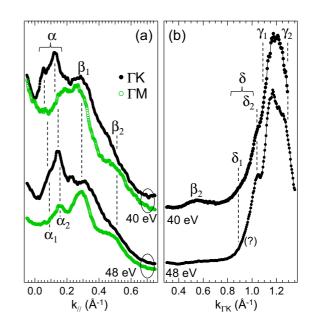

FIG. 23. Direct comparison of MDCs extracted at E_F from Fig. 16 and Fig. 20. The main features of the MDCs are labeled using the same convention as used in Fig. 14.
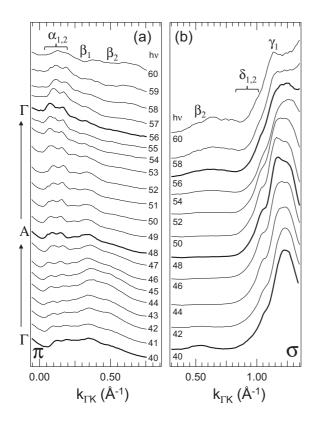
FIG. 24. MDCs extracted at E_F along the ΓK direction using (a) π-polarized and (b) σ-polarized photons. The photon energy was varied from $h\nu = 40$ eV to $h\nu = 60$ eV in steps of 1 eV (a) or 2 eV (b).

providing a possible rationale for the presence of the splitting in $Cr_{1/3}NbS_2$. Further investigations are clearly needed to elucidate the origin of the bands splitting.

The MDCs at E_F shown in Fig. 23(b) also reveal a small, but noticeable, structure located at $\approx 0.50\,\text{Å}^{-1}$ that we identify as the β_2 band. Since the data were collected in σ-polarization geometry, the β_2 band has thus some partial in-plane character ($d_{xy}/d_{x^2-y^2}$). This is consistent with the result of DFT calculations in $2H$-NbSe$_2$, according to which the orbital character changes from d_{z^2} at the center (Γ) to $d_{x^2-y^2}/d_{xy}$ at the corners (K) of BZ.

The photon energy dependence of MDC cuts along the ΓK direction in π- and σ-polarization geometry is shown in Fig. 24. These plots are representative of the dispersion along the vertical k_z direction. Spectra taken with photon energy of 40 and 56 eV are representative of the zone center (Γ point), while those taken at 48 eV are representative of the top of the zone (A point). For the conversion of the photoelectron kinetic energy to the momentum scale, an inner potential of 14 eV was used. In both polarizations, the dispersion along the k_z direction of all of the bands is overall very modest, with k_F changing $\approx 0.05\,\text{Å}^{-1}$ at most, i.e., $\approx 4\%$ of the length of the ΓK vector. The small k_z dispersion of the bands indicates that Cr atoms intercalation does not substantially alter the two-dimensional character of the NbS$_2$ electronic structure. Notably, the measured k_z dispersion represents one of the more significant discrepancies with DFT calculations of $Cr_{1/3}NbS_2$ [29]. The extremely weak k_z dispersion is surprising in light of

the notion that Cr intercalation, which results in the presence of the β_1 and β_2 bands with predominant out-of-plane character, is expected to increase the interaction between NbS$_2$ layers. The data suggest instead that the covalency of the Cr bonds along the c direction is not as strong as predicted by the DFT calculations. This is consistent with the weak intensity of the replica or backfolded bands found at the Γ point (cf. Fig. 19). Indeed, the intensity of such bands is proportional to the strength of the coupling with the superlattice potential [63]. In the case of $Cr_{1/3}NbS_2$, such coupling is due to the interlayer interaction between the NbS$_2$ and Cr layers. The reduced covalency of the bonds along the c direction provides also a rationale for another significant discrepancy with the results of DFT calculations in $Cr_{1/3}NbS_2$ [29]. Due to the presence of the ($\sqrt{3}\times\sqrt{3}$) superstructure of the Cr atoms, the DFT calculations for $Cr_{1/3}NbS_2$ were legitimately carried out in the reduced ($\sqrt{3}\times\sqrt{3}$) BZ, denoted by the dotted hexagon in Fig. 19(a) [29]. There is agreement with the results of the DFT calculations regarding the number of bands crossing E_F at the Γ point, but not with the band dispersion. Our data evidently indicate that the proper BZ for $Cr_{1/3}NbS_2$ is the (1×1) BZ of NbS$_2$. If the electronic structure of $Cr_{1/3}NbS_2$ were correctly described in the reduced ($\sqrt{3}\times\sqrt{3}$) BZ, the Γ and K points would coincide. On the contrary, our data reveal that the states at the Γ and K points are completely different from each other, with the bands having distinct topologies, Fermi crossings, and orbital character. This is clear indication that the coupling between the NbS$_2$ and Cr layers is not strong enough to backfold the electronic structure of $Cr_{1/3}NbS_2$ into the reduced ($\sqrt{3}\times\sqrt{3}$) BZ.

The overestimation of the three dimensionality of the FS and the related weaker interlayer interaction between the NbS$_2$ and Cr layers, stand out as the most significant disagreements between DFT calculations and the experimental results available thus far. In fact, several predictions made concerning the magnetic and electronic properties of $Cr_{1/3}NbS_2$ are found to be consistent with experiments. This includes a saturation magnetic moment of $3.01\,\mu_B$/Cr, fairly close to the experimental value of $3.2\,\mu_B$/Cr [29], and a "bare" low-temperature DOS of $2.76\,\text{eV}^{-1}$ unit cell, which is near the experimental value of $3.40\,\text{eV}^{-1}$ unit cell [29]. Considering that the latter value includes the effective mass enhancement due to such factors as the electron-phonon interaction, it is expected that it is greater than the theoretical value.

It is, thus, important to understand the origin of the disagreements revealed in this paper. The calculated plasma frequencies for $Cr_{1/3}NbS_2$ in the magnetic ground state are 0.95 eV (planar) and 1.12 eV (axial, along c axis). This latter value is indicative of strong three dimensionality, as illustrated in the substantial c axis dispersion in Fig. 11(a) of Ref. [29]. Yet, the results described in the present paper show very little axial dispersion. This suggests that the problem stems from an inadequate description of c axis transport. Since the Cr atom is the only "bridge" between the otherwise well separated NbS$_2$ layers, all interlayer electronic transport occurs through the Cr atom.

Some basic considerations of our first principles calculations suggest a plausible origin of the overstatement of the interlayer Cr-mediated interaction. The DFT-calculated
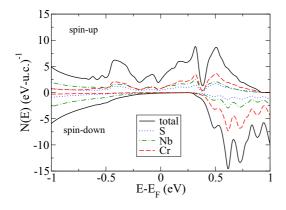
FIG. 25. Calculated spin-polarized DOS of $Cr_{1/3}NbS_2$ in units of inverse electron volts per unit cell. Note the lower values of the DOS for the spin down channel for energies of $\sim \pm 250$ meV from E_F.

magnetic DOS of $Cr_{1/3}NbS_2$ is shown in Fig. 25. Details of these calculations are reported in Refs. [28,29]. Nearly all the spectral weight at E_F is concentrated in the spin-up channel, and in fact, the spin-down channel has a gap just above E_F. From these calculations, one can also extract the plasma frequency squared Ω_p^2 for the separate channels. For the spin-up channel, the planar value of Ω_p^2 is roughly an order of magnitude larger than for the c axis, but surprisingly for the spin down channel, it is the c axis Ω_p^2 that is larger. If the interlayer interaction is just slightly overstated, as the Cr electronic wave functions is found to decay exponentially into the NbS_2 layers, it is quite possible that the gap in the spin-down DOS would extend to E_F, resulting in a strong suppression of the interlayer transport. Furthermore, this overstatement effect would only *increase* the anisotropy in the spin-up channel. We propose this mechanism as a plausible origin of the discrepancy between theory and experiment in $Cr_{1/3}NbS_2$.

V. CONCLUSIONS

The electronic structure of the CHM $Cr_{1/3}NbS_2$ has been studied with PES and ARPES. The surface of $Cr_{1/3}NbS_2$ exposed by *in situ* cleaving possesses a stoichiometry and an atomic ordering that is different from that in the bulk. Specifically, the surface consists of S terminated regions with periodic order, with residual Cr atoms not periodically ordered. The residual Cr atoms randomly distributed on the surface have been identified with ResPES as the origin of the nondispersing states located $\approx 0.5-2$ eV below E_F observed in ARPES data taken with photons of 40 and 48 eV. Despite the presence of disordered areas on the surface, the ARPES data are of high quality and reveal the presence of dispersing bands. The LEED images exhibit intense spots corresponding to the 1×1 periodicity of the NbS_2 lattice and $(\sqrt{3} \times \sqrt{3})R30°$ superstructure spots of weaker intensity originating from subsurface ordering of the Cr atoms with the same periodicity as in the bulk. The ARPES data appear to be consistent with the results of the more bulk sensitive SX-ARPES experiments carried out at higher photon energies. Differences between the data taken at different photon energies are more easily explained as a result of the variation of the matrix elements,

rather than suggesting intrinsic major differences of the electronic structures representative of different probing depths. Even though the Cr atoms on the surface of $Cr_{1/3}NbS_2$ are disordered and occupy sites with a lower symmetry, salient features of the electronic structure revealed by low energy ARPES, such as band dispersion and Fermi momenta, are not significantly modified as compared to the bulk. Further confirmation of this statement derives from the observation of a band replica at the Γ point of the bands found at the K point in both conventional ARPES and SX-ARPES experiments. The possibility of observing band replicas at the Γ point is a direct consequence of the superlattice potential due to the $(\sqrt{3} \times \sqrt{3})R30°$ superstructure of the Cr atoms in the bulk.

A direct comparison of PES and ARPES data in NbS_2 and $Cr_{1/3}NbS_2$ shows unambiguous evidence that Cr intercalation results in a transfer of electron charge from Cr to the NbS_2 layers. Specifically, the $Cr_{1/3}NbS_2$ VB and the S $3s$ shallow core level PES spectra are shifted by ≈ 0.4 eV to higher BE as compared to NbS_2. The same conclusion is inferred from ARPES data taken along the ΓK direction. A comparison of the Nb $3d$ PES core level spectra of NbS_2 and $Cr_{1/3}NbS_2$ reveals a difference in the line shape, indicating that the local electronic environment of the Nb atoms in $Cr_{1/3}NbS_2$ and NbS_2 is different. The suppression of the poorly screened satellite in favor of the well-screened main peak in $Cr_{1/3}NbS_2$ is consistent with the notion that the available screening charge in the NbS_2 layers is increased upon Cr intercalation. Consistent with this body of data, a comparison of the FS shows that in $Cr_{1/3}NbS_2$ the size of the hole pocket at the Γ and K points is reduced. From the ARPES data in NbS_2, two bands, identified with the bilayer split Nb $4d$ bands, were found to cross the Fermi level (E_F) both at the Γ and K points. Of these two bands, one band was found to sink ≈ 0.2 eV below E_F in $Cr_{1/3}NbS_2$. This was rationalized in terms of complete filling of the bonding band due to the added electron carriers introduced by Cr intercalation.

Although it is evident that Cr intercalation donates electrons to the NbS_2-derived bands, the data also reveal that the electronic structure of $Cr_{1/3}NbS_2$ does not derive from that of NbS_2 according to a rigid band shift. In fact, the electronic structure of $Cr_{1/3}NbS_2$ is characterized by the presence of two sets of bands ($\beta_{1,2}$ at Γ and $\delta_{1,2}$ at K) that are not originally present in NbS_2 but emerge instead upon Cr intercalation. Given that the data were taken at a temperature lower than the magnetic transition temperature T_C, we have speculated that both the β and the δ bands are exchange-split bands.

The data provide further evidence that the electronic structure of $Cr_{1/3}NbS_2$ is profoundly modified with respect to that of NbS_2. The NbS_2-derived antibonding band (α band) crossing E_F at the Γ point is split. As this splitting was not observed in NbS_2, we have tentatively assigned the origin of the splitting as a consequence of the lack of inversion symmetry, which occurs in $Cr_{1/3}NbS_2$ but not in NbS_2. Additional important differences in the electronic structure of NbS_2 and $Cr_{1/3}NbS_2$ are observed in the results of polarization-dependent ARPES experiments. On the one hand, the bands crossing E_F at the Γ and the K point in $Cr_{1/3}NbS_2$ were found to have a predominant out-of-plane (d_{z^2}) and in-plane character ($d_{xy}/d_{x^2-y^2}$), respectively. The identified orbital character of the bands at Γ and K is consistent with *ab initio* DFT calculations for $2H$-$NbSe_2$ [45]. On the

other hand, the data taken in σ-polarization geometry reveal an accentuated contribution to the spectra of the bonding band ≈ 0.2 eV below E_F in proximity of the Γ point, particularly evident when the photon energy ($h\nu = 48$ eV) resonates with the BE of the Cr $3p$ core level. Although providing further indication that Cr atoms intercalation results in filling the bonding band derived from NbS$_2$, the data also reveal that the bonding band has orbital character at the Γ point consistent with d_{xy} and/or $d_{x^2-y^2}$. This is in marked contrast to the d_{z^2} character of the bands at the Γ point as expected from the results of DFT calculations of NbSe$_2$ [45]. We have rationalized this discrepancy as an inversion of the energy hierarchy of the a_1' state (with symmetry d_{z^2}) and the e' states ($d_{x^2-y^2}/d_{xy}$) in the D_{3h} manifold of the trigonal prismatic environment of the Nb atom in NbS$_2$ due to the presence of Cr atoms. The $d_{x^2-y^2}/d_{xy}$ orbital character of the bonding band is, thus, a further indication of significant differences, even at a qualitative level beyond a rigid band shift, of the electronic structures of NbS$_2$ and Cr$_{1/3}$NbS$_2$.

The DFT calculations found in the literature indicated that the electronic structure of Cr$_{1/3}$NbS$_2$ is more complex than that given by simple predictions based on a rigid band shift of the NbS$_2$ band structure [29]. Although the DFT calculations are in somewhat qualitative agreement with our experimental results regarding the number of bands crossing E_F at the Γ point, there are also significant discrepancies. First, the DFT calculations overestimate considerably the three dimensionality of the FS in Cr$_{1/3}$NbS$_2$. The experimental data reveal, on the contrary, that the dispersion along the k_z direction of all of the bands is very weak, indicating that Cr intercalation does not substantially alter the two-dimensional character of the NbS$_2$ electronic structure. This is surprising in light of the notion that Cr intercalation, which results in the presence of the β_1 and β_2 bands with predominant out-of-plane character, is expected to increase the interaction between NbS$_2$ layers. The data suggest instead that the covalency of the Cr bonds along the c direction is not as strong as predicted by the DFT calculations. We have discussed above how the apparently weak covalency of the Cr bonds translates into a weak interlayer interaction between the NbS$_2$ and Cr layers, consistent with the weak intensity of the replica bands found at the Γ point. We have also discussed how the overestimation of the covalency of the Cr bonds is the probable cause of another significant discrepancy between calculations and experiments. Due to the presence of the ($\sqrt{3} \times \sqrt{3}$) superstructure ordering of the Cr atoms, the DFT calculations for Cr$_{1/3}$NbS$_2$ were legitimately carried out in the reduced ($\sqrt{3} \times \sqrt{3}$) BZ. On the contrary, the ARPES

data unmistakably indicate that the proper BZ for Cr$_{1/3}$NbS$_2$ is the (1×1) BZ of NbS$_2$, as revealed by the distinct topologies, Fermi crossings, and orbital characters of the states at the Γ and K points. The low degree of covalency of the Cr bonds prevents the coupling between the NbS$_2$ and Cr layers to be strong enough for the ($\sqrt{3} \times \sqrt{3}$) BZ to be the proper BZ for describing the electronic band structure of Cr$_{1/3}$NbS$_2$.

Additional first principles calculations reported here suggest that a plausible origin of the overstatement of the interlayer Cr-mediated interaction is to be found in the detail mechanisms governing the axial transport. Specifically, the calculations indicate that the spin down channel is responsible for axial transport, as revealed by the higher value of the axial plasma frequency. A slight overstatement of the interlayer interaction could quite possibly shift the gap in the spin-down DOS towards E_F, resulting in a strong suppression of the interlayer transport.

In summary, the electronic structure of the CHM Cr$_{1/3}$NbS$_2$ appears to be far more complex and intriguing than anticipated. The results presented here, and similar studies of this type, are likely to be important in order to provide insights into the connection between the electronic structure and the functional properties of CHMs, spin-textures, and spin-orbit interaction effects in magnetic multilayers and magnetic thin films and to develop a systematic understanding as to how intercalation with $3d$ magnetic atoms serves to modify the electronic structure of the host material in potential technological applications of layered TMDCs.

[1] D. M. Bishop, *Group Theory and Chemistry* (Dover, New York, 1993).

[2] M. Kataoka, Spin waves in systems with long period helical spin density waves due to the antisymmetric and symmetric exchange interaction, J. Phys. Soc. Jpn. **56**, 3635 (1987).

[3] K. Ho, T. Kirkpatrick, Y. Sang, and D. Belitz, Ordered phases of itinerant Dzyaloshinsky-Moriya magnets and their electronic properties, Phys. Rev. B **82**, 134427 (2010).

[4] U. K. Rößler, A. N. Bogdanov, and C. Pfleiderer, Spontaneous skyrmion ground state in magnetic metals, Nature (London) **442**, 797 (2006).

[5] S. Mühlbauer, B. Binz, F. Jonietz, C. Pfleiderer, A. Rosch, A. Neubauer, R. Georgii, and P. Böni, Skyrmion lattice in a chiral magnet, Science **323**, 915 (2009).

[6] X. Z. Yu, Y. Onose, N. Kanazawa, J. H. Park, J. H. Han, Y. Matsui, N. Nagaosa, and Y. Tokura, Real space observation of a two-dimensional skyrmion crystal, Nature (London) **465**, 901 (2010).

[7] W. Münzer, A. Neubauer, T. Adams, S. Mühlbauer, C. Franz, F. Jonietz, R. Georgii, P. Böni, B. Pedersen, M. Schmidt, A. Rosch, and C. Pfleiderer, Skyrmion lattice in the doped semiconductor Fe$_{1-x}$Co$_x$Si, Phys. Rev. B **81**, 041203 (2010).

[8] X. Z. Yu, N. Kanazawa, Y. Onose, K. Kimoto, W. Z. Zhang, S. Ishiwata, Y. Matsui, and Y. Tokura, Near room-temperature formation of a skyrmion crystal in thin-films of the helimagnet FeGe, Nat. Mater. **10**, 106 (2009).

[9] H. Wilhelm, M. Baenitz, M. Schmidt, U. Rößler, A. A. Leonov, and A. A. Bogdanov, Precursor Phenomena at the Magnetic Ordering of the Cubic Helimagnet FeGe, Phys. Rev. Lett. **107**, 127203 (2011).

[10] S. Seki, X. Z. Yu, S. Ishiwata, and Y. Tokura, Observation of skyrmions in a multiferroic material, Science **336**, 198 (2012).

[11] F. Jonietz, S. Mühlbauer, C. Pfleiderer, A. Neubauer, W. Münzer, A. Bauer, T. Adams, R. Georgii, P. Böni, R. A. Duim, K. Everschor, M. Garst, and A. Rosch. Spin transfer torques in MnSi at ultralow current densities, Science **330**, 1648 (2010).

[12] N. Romming, C. Hanneken, M. Menzel, J. E. Bickel, B. Wolter, K. von Bergmann, A. Kubetzka, and R. Wiesendanger, Writing and deleting single magnetic skyrmions, Science **341**, 636 (2013).

[13] C. Pfleiderer and A. Rosch, Condensed-matter physics: Single skyrmions spotted, Nature (London) **465**, 880 (2010).

[14] M. Lee, W. Kang, Y. Onose, Y. Tokura, and N. Ong, Unusual Hall Effect Anomaly in MnSi Under Pressure, Phys. Rev. Lett. **102**, 186601 (2009).

[15] A. Neubauer, C. Pfleiderer, B. Binz, a Rosch, R. Ritz, P. Niklowitz, and P. Böni, Topological Hall Effect in the A Phase of MnSi. Phys. Rev. Lett. **102**, 186602 (2009).

[16] Y. Togawa, T. Koyama, K. Takayanagi, S. Mori, Y. Kousaka, J. Akimitsu, S. Nishihara, K. Inoue, A. S. Ovchinnikov, and J. Kishine, Chiral Magnetic Soliton Lattice on a Chiral Helimagnet, Phys. Rev. Lett. **108**, 107202 (2012).

[17] C. Pappas, Viewpoint: New twist in chiral magnets, Physics **5**, 28 (2012).

[18] I. G. Bostrem, J.-i. Kishine, and A. S. Ovchinnikov, Transport spin current driven by the moving kink crystal in a chiral helimagnet, Phys. Rev. B **77**, 132405 (2008).

[19] A. B. Borisov, J. I. Kishine, I. G. Bostrem, and A. S. Ovchinnikov, Magnetic soliton transport over topological spin texture in chiral helimagnet with strong easy-plane anisotropy, Phys. Rev. B **79**, 134436 (2009).

[20] J. I. Kishine, A. S. Ovchinnikov, and I. V. Proskurin, Sliding conductivity of a magnetic kink crystal in a chiral helimagnet, Phys. Rev. B **82**, 064407 (2010).

[21] I. Dzyaloshinsky, A thermodynamic theory of weak ferromagnetism of antiferromagnetics, J. Phys. Chem. Solids **4**, 241 (1958).

[22] T. Moriya. Anisotropic superexchange interaction and weak ferromagnetism. Phys. Rev. **120**, 91 (1960).

[23] C. D. Hu, The Dzyaloshinskii-Moriya interaction in metals, J. Phys.: Condens. Matter **24**, 086001 (2012).

[24] T. Miyadai, K. Kikuchi, H. Kondo, S. Sakka, M. Arai, and Y. Ishikawa, Magnetic properties of $Cr_{1/3}NbS_2$, J. Phys. Soc. Jpn. **52**, 1394 (1983).

[25] P. Bak and M. H. Jensen, Theory of helical magnetic structures and phase transition in MnSi and FeGe, J. Phys. C. **13**, L881 (1980).

[26] T. Moriya and T. Miyadai, Evidence for the helical spin structure due to antisymmetric exchange interaction in $Cr_{1/3}NbS_2$, Solid State Commun. **42**, 209 (1982).

[27] B. J. Chapman, A. C. Bornstein, N. J. Ghimire, D. Mandrus, and M. Lee, Spin structure of the anisotropic helimagnet $Cr_{1/3}NbS_2$ in a magnetic field, Appl. Phys. Lett. **105**, 072405 (2014).

[28] A. C. Bornstein, B. J. Chapman, N. J. Ghimire, D. G. Mandrus, D. S. Parker, and M. Lee, Out-of-plane spin-orientation dependent magnetotransport properties in the anisotropic helimagnet $Cr_{1/3}NbS_2$, Phys. Rev. B **91**, 184401 (2015).

[29] N. J. Ghimire, M. A. McGuire, D. S. Parker, B. Sipos, S. Tang, J.-Q. Yan, B. C. Sales, and D. Mandrus, Magnetic phase transitions in single crystals of the chiral helimagnet $Cr_{1/3}NbS_2$, Phys. Rev. B **87**, 104403 (2013).

[30] Y. Togawa, Y. Kousaka, S. Nishihara, K. Inoue, J. Akimitsu, A. S. Ovchinnikov, and J. Kishine, Interlayer Magnetoresistance Due to Chiral Soliton Lattice Formation in Hexagonal Chiral Magnet $CrNb_3S_6$, Phys. Rev. Lett. **111**, 197204 (2013).

[31] W. Yao, D. Xiao, and Q. Niu, Valley-dependent optoelectronics from inversion symmetry breaking, Phys. Rev. B **77**, 235406 (2008).

[32] D. Xiao, G.-B. Liu, W. Feng, X. Xu, and W. Yao, Coupled Spin and Valley Physics in Monolyers of MoS_2 and Other Group VI Dichalcogenides, Phys. Rev. Lett. **108**, 196802 (2012).

[33] K. F. Mak, K. He, J. Shan, and T. F. Heinz, Control of valley polarization in monolayer MoS_2 by optical helicity, Nat. Nanotechnol. **7**, 494 (2012).

[34] H. Zeng, J. Dai, W. Yao, D. Xiao, and X. Cui, Valley polarization in MoS_2 monolayers by optical pumping, Nat. Nanotechnol. **7**, 490 (2012).

[35] H. Wang, H. Yuan, S. S. Hong, Y. Li, and Y. Cui, Physical and chemical tuning of two dimensional transition metal dichalcogenides, Chem. Soc. Rev. **44**, 2664 (2015).

[36] H. I. Starnberg, Recent developments in alkali metal intercalation of layered transition metal dichalcogenides, Mod. Phys. Lett. B **14**, 455 (2000).

[37] S. F. Meyer, R. E. Howard, G. R. Stewart, J. V. Acrivos, and T. H. Geballe, Properties of intercalated 2H NbSe$_2$, 4HbTaS$_2$, and 1TTaS$_2$, J. Chem. Phys. **62**, 4411 (1975).

[38] S. E. Stoltz, H. I. Starnberg, and L. J. Holleboom, Rb intercalation of 1T-TaSe$_2$ studied by photoelectron spectroscopy, Phys. Rev. B **67**, 125107 (2003).

[39] E. Morosan, H. W. Zandbergen, B. S. Dennis, J. W. G. Bos, Y. Onose, T. Klimczuk, A. P. Ramirez, N. P. Ong, and R. J. Cava, Superconductivity in $Cu_x TiSe_2$, Nat. Phys. **2**, 544 (2006).

[40] R. H. Friend and A. D. Yoffe, Electronic-properties of intercalation complexes of the transition-metal dichalcogenides, Adv. Phys. **36**, 1 (1987).

[41] M. Kertesz and R. Hoffmann, Octahedral vs. trigonal-prismatic coordination and clustering in transition-metal dichalcogenides, J. Am. Chem. Soc. **106**, 3453 (1984).

[42] S. S. P. Parkin, E. A. Marseglia, and P. J. Browns, Magnetic structure of $Co_{1/3}NbS_2$ and $Co_{1/3}TaS_2$, J. Phys. C **16**, 2765 (1983).

[43] F. Hulliger and E. Pobitschka, On the magnetic behavior of new 2H-NbS$_2$-type derivatives, J. Solid State Chem. **1**, 117 (1970).

[44] S. S. P. Parkin and R. H. Friend, 3d transition metal intercalates of the niobium and tantalum dichalcogenides. I. Magnetic properties, Philos. Mag. B **41**, 65 (1980).

[45] D. W. Bullett, Electronic band structure and bonding in transition metal dichalcogenides by atomic orbital methods, J. Phys. C **11**, 4501 (1978).

[46] R. Corcoran, P. Meeson, Y. Onuki, P.-A. Probst, M. Springford, K. Takita, H. Harima, G. Y. Guo, and B. L. Gyorffy, Quantum oscillations in the mixed state of the type II superconductor, 2H-NbSe$_2$, J. Phys.: Condens. Matter **6**, 4479 (1994).

[47] Th. Straub, Th. Finteis, R. Claessen, P. Steiner, S. Hüfner, P. Blaha, C. S. Oglesby, and E. Bucher, Charge-Density-Wave Mechanism in 2H-NbSe$_2$: Photoemission Results, Phys. Rev. Lett. **82**, 4504 (1999).

[48] K. Rossnagel, O. Seifarth, L. Kipp, M. Skibowski, D. Voß, P. Krüger, A. Mazur, and J. Pollmann, Fermi surface of 2H-NbSe$_2$ and its implications on the charge-density-wave mechanism, Phys. Rev. B **64**, 235119 (2001).

[49] S. V. Borisenko, A. A. Kordyuk, V. B. Zabolotnyy, D. S. Inosov, D. Evtushinsky, B. Büchner, A. N. Yaresko, A. Varykhalov, R. Follath, W. Eberhardt, L. Patthey, and H. Berger, Two Energy Gaps and Fermi-Surface "Arcs" in NbSe$_2$, Phys. Rev. Lett. **102**, 166402 (2009).

[50] W. B. Clark, Structural and photoemission studies of some transition metal intercalates of NbS$_2$, J. Phys. C **9**, L693 (1976).

[51] R. H. Friend, A. R. Beal, and A. D. Yoffe, Electrical and magnetic properties of some first row transition metal intercalates of niobium disulphides, Philos. Mag. **35**, 1269 (1977).

[52] K. Rossnagel, E. Z. Totenberg, H. Koh, N. V. Smith, and L. Kipp, Continuous Tuning of Electronic Correlations by Alkali Adsorption on Layered 1T-TaS$_2$, Phys. Rev. Lett. **95**, 126403 (2005).

[53] H. J. Carawak, Y. Tomm, and C. Pettenkofer, Localization and charge density wave transformation in Cs-intercalated 1T-TaSe$_2$, Surf. Sci. **465**, 301 (2000).

[54] C. Battaglia, H. Cercellier, L. Despont, C. Monney, M. Prester, H. Berger, L. Forro, M. G. Garnier, and P. Aebi, Non-uniform doping across the Fermi surface of NbS$_2$ intercalates, Eur. Phys. J. B **57**, 385 (2007).

[55] Y. Saitoh, K. Kobayashi, A. Fujimori, Y. Yamamura, M. Koyano, T. Tsuji, and S. Katayama, Photoemission and core-level absorption spectroscopy of Fe$_x$NbS$_2$, J. Electron Spectrosc. Relat. Phenom. **144-147**, 829 (2005).

[56] W. Liu, D. West, L. He, Y. Xu, J. Liu, K. Wang, Y. Wang, G. van der Laan, R. Zhang, S. Zheng, and K. L. Wang, Atomic-scale magnetism of Cr-doped Bi$_2$Se$_3$ thin film topological insulators, ACS Nano **9**, 10237 (2015).

[57] Z. Dai, Q. Xue, Y. Gong, C. G. Slough, and R. V. Coleman, Scanning-probe-microscopy studies of superlattice structures and density-wave structures in 2H-NbSe$_2$, 2H-TaSe$_2$, and 2H-TaS$_2$ induced by Fe doping, Phys. Rev. B **48**, 14543 (1993).

[58] C. S. Fadley, Looking deeper: Angle-resolved photoemission with soft and hard x-rays, Synchrotron Radiat. News **25**, 26 (2012).

[59] V. N. Strocov, M. Kobayashi, X. Wang, L. L. Lev, J. Krempasky, V. V. Rogalev, T. Schmitt, C. Cancellieri, and M. L. Reinle-Schmitt, Soft-x-ray ARPES at the Swiss Light Source: From 3D materials to buried interfaces and impurities, Synchrotron Radiat. News **27**, 31 (2014).

[60] A. Kuc, N. Zibouche, and T. Heine, Influence of quantum confinement on the electronic structure of the transition metal sulfide TS$_2$, Phys. Rev. B **83**, 245213 (2011).

[61] S. Hüfner, *Photoelectron Spectroscopy. Principles and Applications*, 3rd ed. (Springer, Berlin, 2003).

[62] A. Damascelli, Z. Hussain, and Z.-X. Shen, Angle-resolved photoemission studies of cuprate superconductors, Rev. Mod. Phys. **75**, 473 (2003).

[63] V. Brouet, W. L. Yang, X. J. Zhou, Z. Hussain, N. Ru, K. Y. Shin, I. R. Fisher, and Z. X. Shen, Fermi Surface Reconstruction in the CDW State of Ce Te$_3$ Observed by Photoemission, Phys. Rev. Lett. **93**, 126405 (2004).